

# In situ observation of shear-driven amorphization in silicon crystals

Yang He<sup>1</sup>, Li Zhong<sup>1</sup>, Feifei Fan<sup>2</sup>, Chongmin Wang<sup>3\*</sup>, Ting Zhu<sup>2,4\*</sup> and Scott X. Mao<sup>1\*</sup>

**Amorphous materials are used for both structural and functional applications<sup>1–5</sup>. An amorphous solid usually forms under driven conditions such as melt quenching<sup>4</sup>, irradiation<sup>6</sup>, shock loading<sup>7–9</sup> or severe mechanical deformation<sup>10</sup>. Such extreme conditions impose significant challenges on the direct observation of the amorphization process. Various experimental techniques have been used to detect how the amorphous phases form, including synchrotron X-ray diffraction<sup>11</sup>, transmission electron microscopy (TEM)<sup>12</sup> and Raman spectroscopy<sup>13</sup>, but a dynamic, atomistic characterization has remained elusive. Here, by using *in situ* high-resolution TEM (HRTEM), we show the dynamic amorphization process in silicon nanocrystals during mechanical straining on the atomic scale. We find that shear-driven amorphization occurs in a dominant shear band starting with the diamond-cubic (*dc*) to diamond-hexagonal (*dh*) phase transition and then proceeds by dislocation nucleation and accumulation in the newly formed *dh*-Si phase. This process leads to the formation of an amorphous Si (*a*-Si) band, embedded with *dh*-Si nanodomains. The amorphization of *dc*-Si via an intermediate *dh*-Si phase is a previously unknown pathway of solid-state amorphization.**

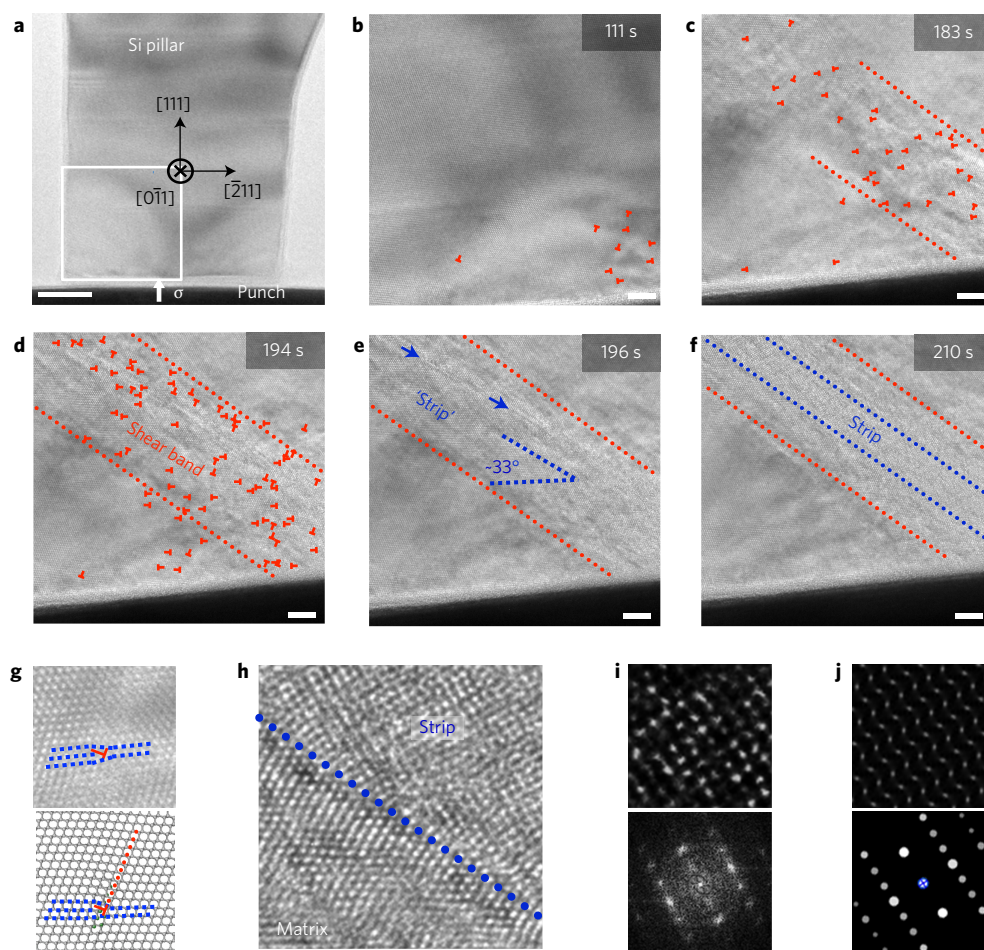
Covalent crystals such as bulk Si are intrinsically brittle at room temperature<sup>14</sup>. They can nonetheless exhibit a transition from the crystalline to amorphous phase during mechanical deformation under pressure confinement, for example, when subjected to large overall hydrostatic pressure<sup>11</sup>, nanoindentation<sup>15–17</sup> and surface scratching<sup>12</sup>. Recent nanomechanical experiments have shown that reducing the size of covalent crystals to the nanoscale can effectively suppress the conventional deformation mode of brittle fracture<sup>18–22</sup>, due to the strong flaw tolerance of nanoscale materials relative to their bulk counterparts. Revealing such a size effect opens up opportunities to study solid-state amorphization without the need for pressure confinement. Moreover, atomistic simulations suggest that the strong localized bonding in covalent crystals could facilitate solid-state amorphization in nanoscale samples free of fracture-producing flaws<sup>23,24</sup>. However, experimental studies of covalent Si nanostructures to date only report crystalline phase transformations and/or plasticity governed by dislocations<sup>18–21,25</sup>. Our *in situ* HRTEM uniaxial compression experiments provide a route to directly observe shear-driven amorphization processes at the atomic scale.

Figure 1a–f and Supplementary Movie 1 show *in situ* compression of a  $\langle 111 \rangle$ -oriented Si nanopillar with a diameter of  $\sim 82$  nm (Fig. 1a) at a strain rate of  $\sim 10^{-3}$  s<sup>-1</sup>. The nanopillar initially underwent elastic deformation upon compression. Plastic deformation then set in by nucleation of dislocations from the contact between the nanopillar and the loading punch (Fig. 1b). The amount of sessile dislocations gradually increased with compression

(Fig. 1c), indicating the trapping of dislocations inside the nanopillar. Based on the measured *d*-spacing of  $\langle 1\bar{1}1 \rangle$  planes at a local region near the contact, we estimated the axial stresses and associated resolved shear stresses during compression (Supplementary Fig. 1). When the applied compressive stress reached  $\sim 14$  GPa, the overall uniform deformation of the nanopillar gave way to localized deformation in a dominant shear band (Fig. 1d). Further development of the shear band was featured with the formation of an internal ‘strip’, as the compressive stress reached  $\sim 18$  GPa. As shown in the HRTEM image in Fig. 1e and Supplementary Fig. 2, the incipient strip exhibited lattice disturbances and was oriented between  $\langle 1\bar{1}3 \rangle$  and  $\langle 1\bar{1}4 \rangle$ , that is, inclined at  $\sim 33^\circ$  to the adjacent  $\langle 1\bar{1}1 \rangle$  plane. During further compression of the nanopillar, the strip gradually thickened and extended (Fig. 1f), driven by an in-plane shear (Supplementary Fig. 2). Interestingly, a new crystalline phase started to form inside the strip, with a lattice structure different from that of the *dc*-Si matrix (Fig. 1f).

Our *in situ* HRTEM imaging revealed the atomic-scale details of deformation-induced dislocations and phase transformation. Dislocations that initially formed during the incipient plastic deformation (Fig. 1b,c) were of the perfect type on  $\{111\}$  planes (Fig. 1g), instead of partials that would otherwise drag long stacking faults. The atomic core structure of these dislocations cannot be determined exactly from HRTEM images. Hence, it remains unclear if they are shuffle or glide-set  $\{111\}$  dislocations. However, the dislocation core structure in HRTEM images is close to that obtained in our molecular dynamics (MD) simulations (see Supplementary section ‘MD procedures’), which produced full dislocations on the  $\{111\}$  shuffle planes (Fig. 1g). The characteristic shear stresses for the onset of dislocation nucleation and subsequent dislocation glide were estimated from the first major load drop (Supplementary Fig. 1) to be  $\sim 2$  and  $\sim 1$  GPa, respectively. These stresses are consistent with the previous theoretical predictions<sup>26</sup> and with estimates from *ex situ* experiments on shuffle-set dislocation<sup>27</sup>. In addition, our MD simulations indicate that trapping of dislocations inside the nanopillar can be primarily attributed to the interlocking of dislocations on three equivalent  $\{111\}$  planes inclined at  $\sim 19.5^\circ$  to the  $\langle 111 \rangle$  loading axis. Back stresses from these trapped dislocations presumably slowed down the rate of dislocation nucleation as well as the movement of nucleated dislocations from the contact interface. As a result, the nanopillar gradually hardened during continued compression, as evidenced by the measured stress–strain response (Supplementary Fig. 1). The HRTEM image and its fast Fourier transform analysis (Fig. 1h–j) show that the newly formed crystalline phase in the strip is *dh*-Si viewed from the  $\langle 11\bar{2}0 \rangle$  axis; it is a 2H polytype of *dc*-Si with the stacking sequence ...AaBbAaBb... along the  $\langle 111 \rangle$  direction and is also known as Si-IV or wurtzite Si (ref. 28). It was previously suggested that *dc*- to *dh*-Si

<sup>1</sup>Department of Mechanical Engineering and Materials Science, University of Pittsburgh, Pittsburgh, Pennsylvania 15261, USA. <sup>2</sup>Woodruff School of Mechanical Engineering, Georgia Institute of Technology, Atlanta, Georgia 30332, USA. <sup>3</sup>Environmental Molecular Sciences Laboratory, Pacific Northwest National Laboratory, Richland, Washington 99352, USA. <sup>4</sup>School of Materials Science and Engineering, Georgia Institute of Technology, Atlanta, Georgia 30332, USA. \*e-mail: [sxm2@pitt.edu](mailto:sxm2@pitt.edu); [ting.zhu@me.gatech.edu](mailto:ting.zhu@me.gatech.edu); [chongmin.wang@pnnl.gov](mailto:chongmin.wang@pnnl.gov)



**Figure 1** | *In situ* TEM observation of deformation-induced dislocations and phase transformation in a  $\langle 111 \rangle$ -oriented Si nanopillar under compression.

**a**, Overview of a nanopillar under compression by a punch. Scale bar, 20 nm. The box indicates the region where the HRTEM images in **b–f** were taken. **b–d**, Time-lapse TEM images showing formation of a dominant shear band via accumulation of dislocations inside the shear band. **e, f**, Subsequent TEM images showing formation of a strip of *dh*-Si in the central region of the shear band. Scale bars in **b–f**, 5 nm. The red and blue dotted lines mark the boundaries of the shear band and *dh*-Si strip, respectively. Arrows indicate the incipient strip. **g**, Comparison between the HRTEM and MD images of a full dislocation on the  $\{111\}$  slip plane (indicated by red dotted line). **h**, HRTEM image of the interface between the strip and the matrix. **i**, HRTEM image and corresponding fast Fourier transform of the *dh*-Si phase in the strip. **j**, Simulated HRTEM image and fast Fourier transform of *dh*-Si along the  $[11\bar{2}0]$  axis.

phase transformation could be accomplished by a secondary deformation twinning in a pre-existing twin<sup>29</sup>. In contrast, no pre-existing or deformation twins were observed during our experiments. Our observation of *dh*-Si nucleation and growth indicated that *dc*- to *dh*-Si phase transformation occurred in the highly sheared *dc* 'strip' (Supplementary Figs 2 and 3 and Supplementary Discussion 1) and is consistent with the mechanism of martensitic transformation through the  $[5\bar{5}\bar{2}](1\bar{1}\bar{5})_{dc}$  shear proposed in ref. 30.

Shear-driven amorphization inside the *dh*-Si 'strip' occurred during further compression (Supplementary Movie 2), starting with the formation of *a*-Si nanodomains (Fig. 2a,b). Initially, an increasing number of dislocations were built up in the sheared *dh*-Si strip. These dislocations nucleated inside the strip at a characteristic resolved shear stress of  $\sim 6$  GPa and appeared on both the  $\{1\bar{1}00\}$  (dominant) and  $\{0002\}$  planes. During this process, dislocation dipoles were observed. Dislocations within the strip were nearly immobile, so shear of the strip was largely mediated by dislocation nucleation. As a result, the local lattice of *dh*-Si was gradually disrupted, resulting in a nanosized *a*-Si domain (Fig. 2c–h). The crystal lattice around each *a*-Si domain was highly distorted (Fig. 2h). Evidence for this is further provided by fast Fourier transform analysis of the strip (Fig. 2b, inset), which demonstrates the pulverization and large

local rotation of the *dh*-Si lattice resulting from dislocation accumulation and shear flow of the *a*-Si matrix. Hence, the HRTEM images in Fig. 2c–h directly reveal a dynamic amorphization process mediated by the accumulation of immobile dislocation dipoles. During this process, the local dislocation density kept increasing, from  $\sim 3 \times 10^{12} \text{ cm}^{-2}$  (Fig. 2c) to  $3 \times 10^{13} \text{ cm}^{-2}$  (Fig. 2g).

Expansion and coalescence of the *a*-Si domains during further shearing of the *dh*-Si strip resulted in a fully developed amorphous band embedded with residual nanosized *dh*-Si domains (Fig. 3a). Importantly, amorphization occurred dominantly inside the *dh*-Si strip. This is indicated by the fact that *a*-Si only existed within the *dc*-Si/*dh*-Si interface, with the *dc*-Si phase outside the strip remaining undisrupted, implying that the formation of the intermediate *dh*-Si phase was a necessary step of amorphization. Further evidence is provided by selected area electron diffraction (SAED) of the deformed nanopillar, where the *dc* structure remained well-defined (indicated by sharp diffraction spots in the inset of Fig. 3b), while the *dh* structure was pulverized (rings in the inset of Fig. 3b). Interestingly, the diffraction intensity profiles of *a*-Si formed via shear-driven amorphization are different from those of *a*-Si vitrified from a Si melt (Fig. 3b), implying their different structures. Our statistical analysis of diffraction profiles further

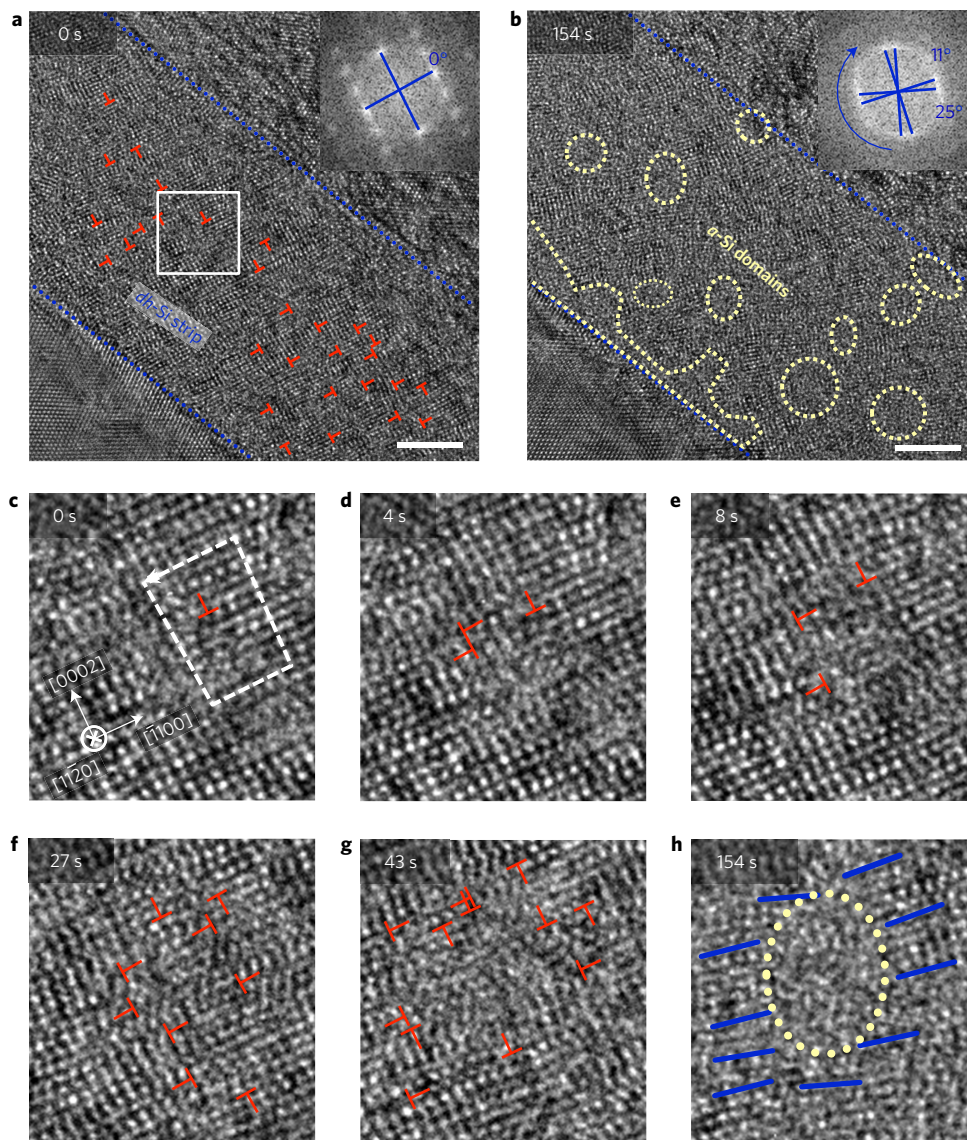


**Figure 2 | Shear-driven amorphization in a *dh*-Si strip. **a****, HRTEM image of the *dh*-Si strip before formation of amorphous domains. **b**, HRTEM image showing formation of nanosized amorphous domains (marked by dotted circles). Scale bars in **a,b**, 5 nm. Insets (**a,b**): fast Fourier transform of the strip, with blue crosses tracking the rotation of the *dh*-Si lattice, and the *dh*-Si lattice in the strip pulverized and rotated during the shear-driven amorphization process. **c–h**, Time-lapse HRTEM images of the boxed region in **a**, showing the atomic-scale process of formation of an amorphous domain via dislocation accumulation. Dashed lines and arrow in **c** indicate the Burgers circuit and Burgers vector, respectively. The blue lines in **h** mark the individual basal planes around the amorphous domain (indicated by a dotted circle).

confirmed this difference (Supplementary Fig. 4). Note that the diffraction intensity profile of *a*-Si formed via shear-driven amorphization was extracted from SAED by subtracting the sharp diffraction spots from *dc*-Si and the rings from *dh*-Si. The profile exhibited ‘bumps’ that lie close to the positions of the diffraction rings from polycrystalline *dh*-Si rather than those from *dc*-Si. Hence, the shear-induced *a*-Si phase in the present study was probably transformed from *dh*-Si.

It is worth noting that the structure of *a*-Si was previously described by a paracrystalline model<sup>3,31</sup>. Distinct from the conventional continuous random network motif, the paracrystalline *a*-Si model contains local topological orders of ~1–2 nm scale in the random network matrix, supported by localized diffractions<sup>3,32</sup>. However, it has been difficult to determine the exact structure of local ordering in the paracrystalline model of *a*-Si. Our *in situ* atomic-scale observation directly revealed the dynamic structural transformation from *dc*-Si to *a*-Si via *dh*-Si. The remnant nanosized

*dh*-Si domains within the *a*-Si band (Fig. 3a) could correspond to the ordered regions in the paracrystalline model of *a*-Si and thus may provide an atomic structure basis for paracrystalline *a*-Si. In addition, it has previously been reported that the mechanically induced *a*-Si can be annealed to *dh*-Si at ~200–400 °C (refs 13,15). This report is consistent with our finding of remnant *dh*-Si domains in *a*-Si, which may serve as a nucleus of crystal growth of *dh*-Si from *a*-Si, leading to the annealed product of *dh*-Si at elevated temperatures.

A loading orientation effect on shear-driven amorphization was revealed during compression of a <100>-oriented Si nanopillar. Figure 4 and Supplementary Movie 3 show the compression responses of a <100> nanopillar, which were dominated by the nucleation and glide of partial dislocations. This nanopillar had a diameter of ~86 nm (Fig. 4a) and was compressed at a strain rate of ~10<sup>-3</sup> s<sup>-1</sup>. The majority of dislocations formed were {111} partials with stacking faults behind (Fig. 4b). These partials glided on

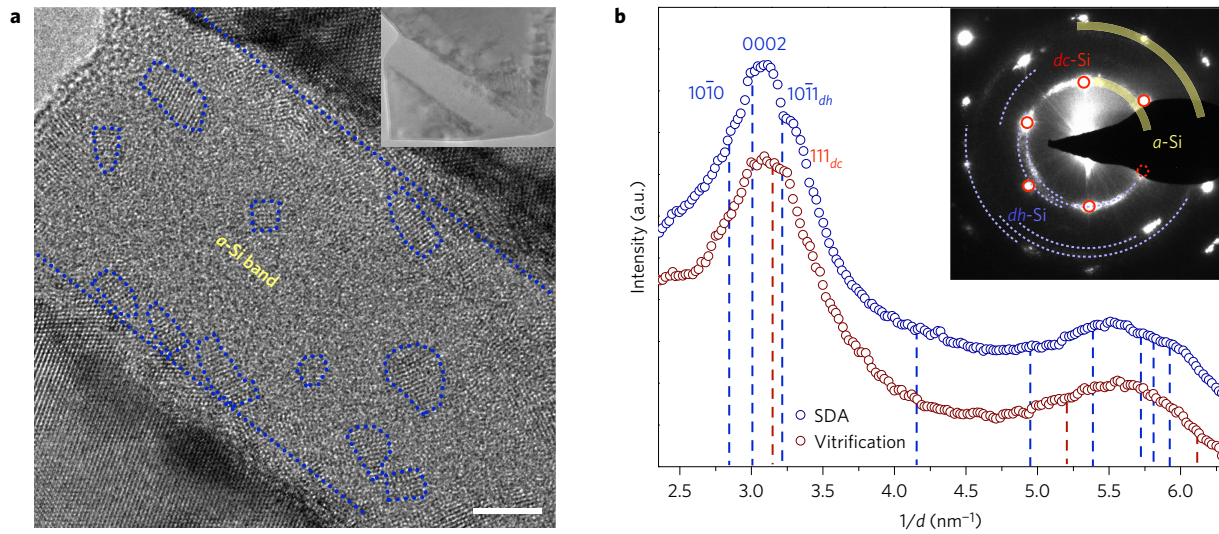


**Figure 3 | Atomic structures in a fully developed  $\alpha$ -Si shear band.** **a**, HRTEM image of the  $\alpha$ -Si shear band containing a number of residual nanosized  $dh$ -Si clusters (marked by dotted circles). Scale bar, 5 nm. Inset **(a)**: overview of a deformed  $\langle 111 \rangle$  nanopillar. **b**, Diffraction intensity profile of  $\alpha$ -Si (blue, extracted from the SAED pattern in the inset), compared with that from vitrified Si (red). The intensity profile corresponding to  $\alpha$ -Si formed via shear-driven amorphization (SDA) has been shifted upwards by a constant to facilitate a comparison of two intensity profiles. Blue rings (in the SAED pattern) and dashed lines (in the intensity profile) mark the diffraction positions of polycrystalline  $dh$ -Si. Red circles (in the SAED pattern) and dashed lines (in the intensity profile) mark the diffraction positions of  $dc$ -Si. Yellow rings (in the SAED pattern) mark the diffraction halo of  $\alpha$ -Si.

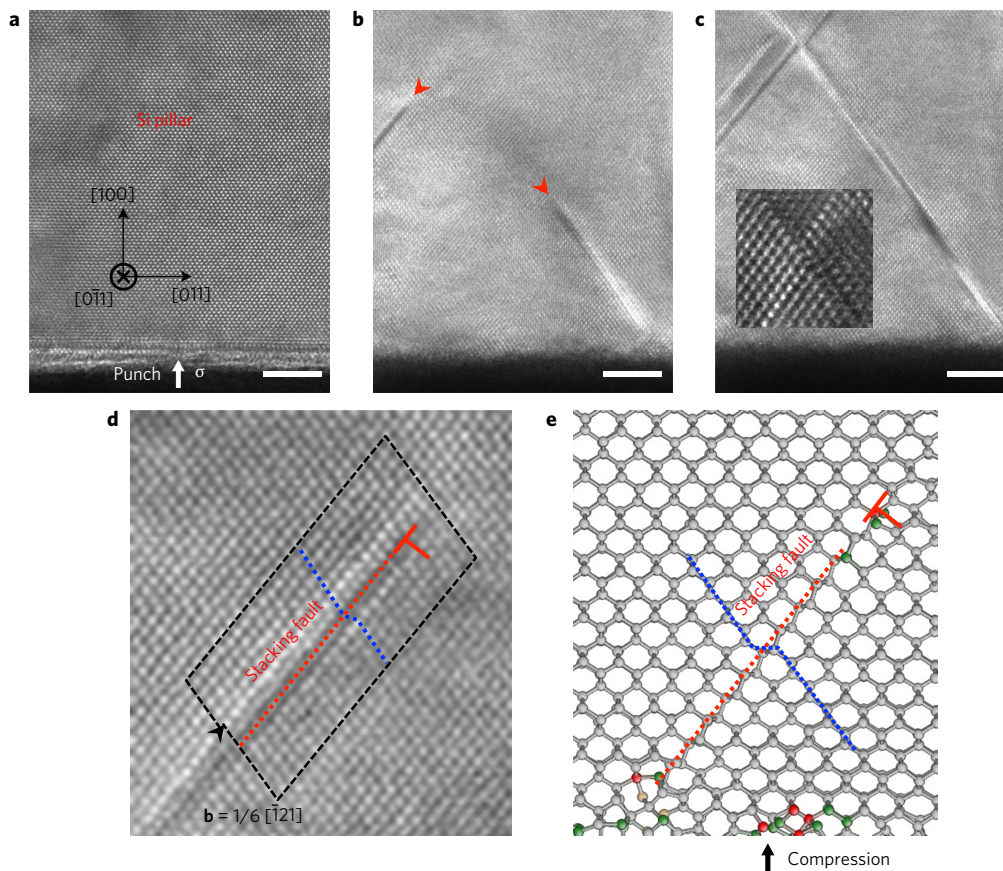


**Figure 4 | Deformation-induced partial dislocations in a  $\langle 100 \rangle$ -oriented Si nanopillar under compression.** **a**, HRTEM image of a pristine nanopillar. **b**, Nucleation of partial dislocations (indicated by arrow heads) on symmetric  $\{111\}$  slip planes. **c**, Intersection and crossing of two partials. Inset: local atomic structure near two intersecting partials. Scale bars in **a-c**, 5 nm. **d**, Analysis of the Burgers vector of  $1/6\{111\}\langle 112 \rangle$  (indicated by arrow head) for a partial dislocation with a stacking fault in an HRTEM image. Black dashed lines represent the Burgers circuit. **e**, MD image showing a  $1/6\{111\}\langle 112 \rangle$  partial nucleated from the compressed region at the bottom. The red dotted line indicates a stacking fault on the glide-set  $\{111\}$  slip plane. Gliding of this stacking fault causes a deflection in the intersecting  $\{111\}$  slip plane, highlighted by the blue dotted line.

two equivalent slip systems of  $1/6[12\bar{1}](\bar{1}11)$  and  $1/6[\bar{1}21](11\bar{1})$  (Fig. 4c), as shown by Burgers vector analysis in both HRTEM and MD images (Fig. 4d,e). They frequently intersected and temporarily arrested one another. The resulting dislocation locks were destroyed with further compression, and the released partials glided and eventually escaped from the side faces of the nanopillar (Fig. 4c). These partials were sufficiently active to accommodate the applied strain load, such that amorphization was apparently suppressed. The distinct types of active dislocations in  $\langle 100 \rangle$  and  $\langle 111 \rangle$  nanopillars were shown by our MD simulations (Supplementary Fig. 5) and can be attributed to an effect of maximum Schmid factors on the driving shear stress of surface dislocation nucleation (Supplementary Table 1 and Supplementary Discussion 2). In addition, we note that the Schmid factor of the shear stress that drives phase transformation from *dc*- to *dh*-Si in a  $\langle 100 \rangle$  nanopillar under compression is only half of that in a  $\langle 111 \rangle$  nanopillar. This factor, in conjunction with dominant partial dislocation activities, should be responsible for the lack of phase transition of *dc*- to *dh*-Si and ensuing shear-driven amorphization in the  $\langle 100 \rangle$  nanopillar.

It should be noted that we did not observe phase transition from the initial *dc* to the  $\beta$ -Sn structure (Si-II)<sup>33</sup> in experiments. Si-II often forms during high-pressure compression of Si and, upon unloading, it tends to transform to *a*-Si and/or a mixture of metastable polymorphs of Si-XII and Si-III (refs 15–17), which were absent in the final phase (Supplementary Fig. 6). In addition, it is interesting to point out the influence of deconfined sample geometry on the observed amorphization. The nanopillars (~90 nm in diameter) in our experiments are in a nano-deconfined state because the feature size is less than ~134 nm (ref. 25) and as such prone to dislocation-governed deformation. Indeed, the incipient plastic deformation in our Si nanopillars was controlled by dislocations. Our study shows that at late stages of deformation, the dislocation plasticity in  $\langle 111 \rangle$  nanopillars was insufficient to accommodate the imposed strain load. This led to the formation of a dominant shear band where both the transition of *dc*-Si to *dh*-Si and the subsequent shear-driven amorphization occurred. In this work, we have not systematically varied the nanopillar geometry to determine the critical size below which shear-driven amorphization occurs (this is an important issue that warrants further study in the future).

In conclusion, the shear-driven amorphization inside a dominant shear band of single Si nanocrystals was directly observed in real time with atomic resolution. One implication of this mechanism is that the solid-state amorphization does not necessarily involve direct transformation from the parent crystalline phase to the amorphous product simply through the accumulation of defects. Instead, an intermediate new crystalline phase could form before amorphization. As a result, the amorphous structure formed can consist of distributed nanosized crystals with an intermediate phase such as *dh*-Si. Such structural characteristics could influence the electrical and electrochemical performance of the amorphous products. We believe that our approach can be extended to the study of other mechanically driven deformation mechanisms in a broad class of covalent solids.

## Methods

Methods and any associated references are available in the [online version of the paper](#).

Received 18 March 2016; accepted 10 August 2016;  
published online 19 September 2016

## References

- Johnson, W. L. Thermodynamic and kinetic aspects of the crystal to glass transformation in metallic materials. *Prog. Mater. Sci.* **30**, 81–134 (1986).
- Mott, N. F. Electrons in disordered structures. *Adv. Phys.* **50**, 865–945 (2001).
- Treacy, M. M. & Borisenko, K. B. The local structure of amorphous silicon. *Science* **335**, 950–953 (2012).
- Zhong, L., Wang, J., Sheng, H., Zhang, Z. & Mao, S. X. Formation of monatomic metallic glasses through ultrafast liquid quenching. *Nature* **512**, 177–180 (2014).
- Bauer, J., Schroer, A., Schwaiger, R. & Kraft, O. Approaching theoretical strength in glassy carbon nanolattices. *Nat. Mater.* **15**, 438–443 (2016).
- Takeda, S. & Yamasaki, J. Amorphization in silicon by electron irradiation. *Phys. Rev. Lett.* **83**, 320–323 (1999).
- Gamero-Castaño, M., Torrents, A., Valdevit, L. & Zheng, J. Pressure-induced amorphization in silicon caused by the impact of electrosprayed nanodroplets. *Phys. Rev. Lett.* **105**, 145701 (2010).
- Zhao, S. *et al.* Amorphization and nanocrystallization of silicon under shock compression. *Acta Mater.* **103**, 519–533 (2016).
- Zhao, S. *et al.* Pressure and shear-induced amorphization of silicon. *Extrem. Mech. Lett.* **5**, 74–80 (2015).
- Huang, J. Y., Yasuda, H. & Mori, H. Deformation induced amorphization in ball milled silicon. *Phil. Mag. Lett.* **79**, 305–314 (1999).
- Deb, S. K., Wilding, M., Somayazulu, M. & McMillan, P. F. Pressure-induced amorphization and an amorphous-amorphous transition in densified porous Si. *Nature* **414**, 528–530 (2001).
- Minowa, K. & Sumino, K. Stress-induced amorphization of silicon crystal by mechanical scratching. *Phys. Rev. Lett.* **69**, 320–322 (1992).
- Wu, K., Yan, X. Q. & Chen, M. W. *In situ* Raman characterization of reversible phase transition in stress-induced amorphous silicon. *Appl. Phys. Lett.* **91**, 101903 (2007).
- Cook, R. F. Strength and sharp contact fracture of silicon. *J. Mater. Sci.* **41**, 841–872 (2006).
- Kailer, A., Gogotsi, Y. G. & Nickel, K. G. Phase transformations of silicon caused by contact loading. *J. Appl. Phys.* **81**, 3057–3063 (1997).
- Domnich, V. & Gogotsi, Y. Phase transformation in silicon under contact loading. *Rev. Mater. Sci.* **3**, 1–36 (2002).
- Ruffell, S., Bradby, J. E., Williams, J. S. & Munroe, P. Formation and growth of nanoindentation-induced high pressure phases in crystalline and amorphous silicon. *J. Appl. Phys.* **102**, 063521 (2007).
- Minor, A. M. *et al.* Room temperature dislocation plasticity in silicon. *Phil. Mag.* **85**, 323–330 (2005).
- Han, X. D. *et al.* Low-temperature *in situ* large-strain plasticity of silicon nanowires. *Adv. Mater.* **19**, 2112–2118 (2007).
- Östlund, F. *et al.* Brittle-to-ductile transition in uniaxial compression of silicon pillars at room temperature. *Adv. Funct. Mater.* **19**, 2439–2444 (2009).
- Gerberich, W. W., Stauffer, D. D., Beaber, A. R. & Tymiak, N. I. A brittleness transition in silicon due to scale. *J. Mater. Res.* **27**, 552–561 (2011).
- Wagner, A. J., Hintsala, E. D., Kumar, P., Gerberich, W. W. & Mkhoyan, K. A. Mechanisms of plasticity in near-theoretical strength sub-100 nm Si nanocubes. *Acta Mater.* **100**, 256–265 (2015).
- Huang, S., Zhang, S., Belytschko, T., Terdalkar, S. S. & Zhu, T. Mechanics of nanocrack: fracture, dislocation emission, and amorphization. *J. Mech. Phys. Solids* **57**, 840–850 (2009).
- Zhu, T. & Li, J. Ultra-strength materials. *Prog. Mater. Sci.* **55**, 710–757 (2010).
- Chrobak, D. *et al.* Deconfinement leads to changes in the nanoscale plasticity of silicon. *Nat. Nanotech.* **6**, 480–484 (2011).
- Pizzagalli, L., Godet, J., Guénolé, J. & Brochard, S. Dislocation cores in silicon: new aspects from numerical simulations. *J. Phys.* **281**, 012002 (2011).
- Rabier, J. *et al.* Plastic deformation of silicon between 20 °C and 425 °C. *Phys. Status Solidi C* **4**, 3110–3114 (2007).
- Kasper, J. S. & Wentorf, R. H. Hexagonal (wurtzite) silicon. *Science* **197**, 599 (1977).
- Pirouz, P., Chaim, R., Dahmen, U. & Westmacott, K. H. The martensitic transformation in silicon-I. Experimental observation. *Acta Metall. Mater.* **38**, 313–322 (1990).
- Tan, T. Y., Föll, H. & Hu, S. M. On the diamond-cubic to hexagonal phase transformation in silicon. *Phil. Mag. A* **44**, 127–140 (1981).
- Rudee, M. L. & Howie, A. The structure of amorphous Si and Ge. *Phil. Mag.* **25**, 1001–1007 (1972).
- Borisenko, K. B. *et al.* Medium-range order in amorphous silicon investigated by constrained structural relaxation of two-body and four-body electron diffraction data. *Acta Mater.* **60**, 359–375 (2012).
- Yin, M. T. & Cohen, M. L. Microscopic theory of the phase transformation and lattice dynamics of Si. *Phys. Rev. Lett.* **45**, 1004–1007 (1980).

## Acknowledgements

S.X.M. acknowledges support from the National Science Foundation (NSF, CMMI 1536811) through the University of Pittsburgh. T.Z. acknowledges support from the NSF (DMR 1410331). This work was performed, in part, at the William R. Wiley Environmental Molecular Sciences Laboratory, a national scientific user facility sponsored by the US Department of Energy, Office of Biological and Environmental Research and located at PNNL. PNNL is operated by Battelle for the US Department of Energy (contract no. DE-AC05-76RLO1830). This work was performed in part at the Center for Integrated Nanotechnologies, an Office of Science User Facility operated for the US Department of Energy Office of Science. The authors thank J.Y. Huang for his support on TEM, Z. Zeng for assistance with atomistic simulations and B.M. Nguyen in Los Alamos National Laboratory,

X. Dai in Nanyang Technology University, and S. Krylyuk and A.V. Davydov at the National Institute of Standards and Technology for supplying samples.

### Author contributions

S.X.M., T.Z. and C.M.W. conceived and designed the experiment. Y.H. and L.Z. conducted the TEM experiments. F.F. and T.Z. performed the computer simulations and theoretical analysis. Y.H., T.Z. and S.X.M. co-wrote the paper. All authors discussed the results and commented on the manuscript.

### Additional information

Supplementary information is available in the [online version of the paper](#). Reprints and permissions information is available online at [www.nature.com/reprints](http://www.nature.com/reprints). Correspondence and requests for materials should be addressed to C.W., T.Z. and S.X.M.

### Competing financial interests

The authors declare no competing financial interests.

## Methods

We have developed a novel nanomechanical testing approach that involves a top-down method of sample fabrication and facile nanomanipulation techniques. This approach enables well-controlled loading orientation and *in situ* atomic-resolution characterization of deformation processes. Specifically, Si nanopillars with an axial orientation of  $\langle 111 \rangle$  or  $\langle 100 \rangle$  were made by top-down etching from Si wafers (see Supplementary Methods for details). A piece of Si wafer with nanopillars on its top was then pasted on an aluminium rod with silver glue and fixed on one end of a TEM holder. The loading orientation was adjusted by combining holder rotation and manual handling. The punch was made from an electrochemically etched tungsten tip flattened by a focused ion beam. Driven by a piezo-system on the other end of the TEM holder, the punch compressed the Si nanopillar at a controlled strain

rate. The normal of the punch surface was sometimes not aligned with the pillar axis, so the pillar would be bent under axial loading and hence the lattice image under HRTEM would be lost. Analysis was made for the pillars without obvious bending. More details are provided in the Supplementary Methods and Supplementary Figs 7 and 8. Finally, we note that the intensity of the electron beam was kept low throughout our experiments in order to minimize the beam effect. To evaluate the influence of the electron beam on *in situ* TEM results, we performed beam-blank experiments and observed similar dislocation processes and shear-driven amorphization (Supplementary Fig. 9 and Supplementary Discussion 3). Compared to the compression tests with exposure to the electron beam, a thinner amorphous band formed during beam-blank compression, but with the shear-driven amorphization pathway via *dh*-Si retained.